Remote Sensing of Environment 115 (2011) 1013–1024

Contents lists available at ScienceDirect

Remote Sensing of Environment

journal homepage: www.elsevier.com/locate/rse

Hyperspectral spaceborne imaging of dust-laden flows: Anatomy of Saharan dust storm from the Bodélé Depression

A. Chudnovsky [a,*], A. Kostinski [b], L. Herrmann [c], I. Koren [a], G. Nutesku [d], E. Ben-Dor [d]

[a] Department of Environmental Sciences and Energy Research, Weizmann Institute of Science Rehovot, Israel
[b] Department of Physics, Michigan Technological University, USA
[c] Institute of Soil Science and Land Evaluation (310), University of Hohenheim, D-70593 Stuttgart, Germany
[d] Department of Geography and Human Environment, Tel-Aviv University, Remote Sensing and GIS Laboratory, Israel

ARTICLE INFO

Article history:
Received 2 March 2010
Received in revised form 12 November 2010
Accepted 4 December 2010
Available online 20 January 2011

Keywords:
Atmospheric dust
Mineral dust
Hyperspectral technology
Hyperion satellite
Bodélé Depression

ABSTRACT

We study hyperspectral images of the Bodélé Depression in Northern Chad, acquired by the Hyperion sensor onboard EO-1 spacecraft. Relative abundances of four major mineral components are obtained on a pixel-by-pixel basis and we report on the comparison of images of a dust storm with the same areas on a calm day. Minerals lifted and suspended particles downwind of a dust source are thus identified. Linear Spectral Unmixing (LSU) decomposition results for the calm condition match those of our field study. LSU calm vs. stormy comparison, based on absorbance features, highlight the spectral contrast. Despite low contrast above bright areas, morphological dissimilarity is evident via the wave and tongue-like features, aligned with the prevailing northeasterly winds. We analyze the longest part of shortwave infra-red (2080–2380 nm) wavelengths where the atmosphere is transparent, optical properties are stable, and absorption features of hydroxyl-bearing minerals, sulfates, and carbonates are pronounced. The results of our spectral analyses reveal that clay minerals may be used as tracers for atmospheric dust monitoring even above bright areas. Such clay minerals include kaolinite, illite-moscovite, and Fe-rich nontronite.

1. Introduction and background

The Bodélé Depression in Northern Chad (17° N, 18° E) is the largest source of atmospheric mineral aerosols on Earth (e.g. Prospero et al., 2002; Washington et al., 2003, 2009). The reasons for this include: the strength of the Bodélé Low Level Jet (Washington et al., 2005); the structure of the lowland between the Tibesti (2600 m) and Ennedi (1000 m) massifs, guiding and focusing the surface winds to the Bodélé (Koren et al., 2006); extreme surface gustiness (Goudie, 2009); availability of paleo-lake sediments, including diatomite, for large-scale wind erosion and deflation (Mounkaila, 2006; Schwanghart & Schütt, 2008; Warren et al., 2007; Washington et al., 2006).

Mineral dust particles are lifted into the atmosphere during frequent wind erosion events (Claquin et al., 1999; Tegen & Kohfeld, 2006). The dust particles lifted from a specified location are likely to have composition similar to finer particles (called potential dust fraction, Herrmann, 1996) found in nearby soils or sediments. Dust samples originating from the Bodélé Depression are generally dominated by quartz, with admixtures of clay minerals and Fe-oxyhydrates. The samples contain abundant freshwater Aulacoseira diatoms eroded from desiccated lake deposits (Moreno et al., 2006). Finer grain size fractions are more phyllosilicate-rich (illite, kaolinite, and montmorillonite) and contain higher concentrations of Al, Na, Mg, and Fe (Castillo et al., 2008; Herrmann et al., 2009; Moreno et al., 2006).

Hyperspectral images contain high resolution spectral curve for each of the image pixels. This adds to conventional tools of surface mapping the absorption bands, characteristic of mineral species (Goetz, 2009). Imaging spectrometry (IS) is typically used in surface mineral mapping where ground validation is possible. Such validation is not possible for dust storms because of their transient nature and poor access. Moreover, there is a problem of contrast, particularly in the immediate vicinity of the dust source above bright areas, where it is difficult to separate contribution of the dust plume from that of the underlying surface. Even if there are spectral differences between the suspended dust and the underlying surface, one has to separate effects due to composition from effects that are due to size distribution differences. Yet, tracking entrainment and deposition of dust in a low topographic area associated with strong winds and high sediment supply could be an exciting application of IS. Is it feasible?

To that end, Chudnovsky et al., 2009, used the Hyperion sensor onboard EO-1 spacecraft to study three representative surface areas (covering 60×120 m) over Bodélé Depression, Chad, during calm weather conditions and during a stormy day. Atmospheric dust spectra downwind of Bodélé revealed striking differences in absorption signatures across the longest wavelengths range of shortwave

* Corresponding author. Current address: Harvard School of Public Health, Boston, USA. Tel.: +1 617 3848846.
E-mail address: achudnov@hsph.harvard.edu (A. Chudnovsky).

0034-4257/$ – see front matter © 2010 Elsevier Inc. All rights reserved.
doi:10.1016/j.rse.2010.12.006

infra red (2080–2380 nm) from those of underlying surface, thus providing evidence for mineral-based tracking of atmospheric dust. The atmospheric gas content is almost transparent at this range and distinct absorption features of hydroxyl-bearing minerals, sulfates, and carbonates are presented (common to many petrographic units of the study area).

Here, we substantially extend the analysis by applying pixel-by-pixel comparison of calm vs. stormy conditions. We ask: What are the differences in mineralogical composition of calm and stormy conditions, as indicated by spectral (IS) signature? Is it possible to monitor atmospheric dust over the source area, despite relatively low spectral contrast?

2. Study area

We compare two images of the same area, collected during calm and dust storm conditions. The area of comparison is highlighted in Fig. 1 by dashed red lines at the center of the original Hyperion image (acquired on June 21, 2003 on a calm day), overlaying on a mosaic of two LANDSAT images (acquired on June 2001 and August 2000) over the Bodélé Depression.

The Bodélé Depression in Northern Chad was once part of the largest lake in Africa (Drake & Bristow, 2006). The lake bed is now dry with the exception of Lake Chad in the southern basin. Topography in and around the Bodélé area is varied: flat in the east, rugged in the north-east, cuesta shaped in the north and frequent yardang and dispersed (barchan) dune fields within. Petrography is dominated by eolian sands, lacustrine sediments (including diatomite) and (coarse) sandstones. The former is of Holocene and the latter of tertiary age (Herrmann et al., 2009). Diatomites occur as large surfaces within the Bodélé and as dispersed outcrops in its surroundings, reaching a few meters in thickness (Chappell et al., 2008; Drake & Bristow, 2006; Herrmann et al., 2009; Warren et al., 2007; Wright, 1985). With respect to surfaces, three major types can be distinguished: moving sands (as sheets or dunes), lacustrine sediments (including diatomites) in erosion and desert pavement/serir (Herrmann et al., 2009). Serir surfaces prevail around the Bodélé, lacustrine sediments within, and sands are ubiquitous throughout. Between approximately 15 and 16°N, extended spots of whitish lacustrine sediments occur also eastward of the central basin. Further north (16–17°N) dunes of barchans types, sand sheets, as well as diatomites and swamp ores occur. Surfaces of serir type at eastern fringes of the depression have a dark red, dark brown or even black appearance, which was assumed by Herrmann et al. (2009) to be related to potentially Fe-rich sandstone outcrops. Approximately at 18°N–18°E, variable sediments occur: dunes, lacustrine sediments, and lacustrine sediments overlaying orange-brown dune sands and thin white carbonate crusts embedded in weakly consolidated siltstone. The Bodélé Depression itself is dominated by vast occurrences of lacustrine sediments. Yardang fields, with single yardangs up to 2 m high, mark the ongoing deflation. Northwards of the Depression the surface area is characterized by silty sediments and Fe-sandstones indicating strong Fe-translocation in the paleoenvironment (Herrmann et al., 2009).

2.1. Field samples

Eight reference samples were collected from the area (Fig. 1, Tables 1 and 2) during an expedition in 1997 as a part of the German Climate Research Program (DEKLIM). Stratified samples were collected on-site. After reconstruction of the surface features in the laboratory spectral reflectances in the range 320–2500 nm were measured in the BGR laboratory Hannover with an IRIS (Infra-Red Intelligent Spectroradiometer) radiometer, (Mounkaila, 2006) against a white baryta paper as reference material. Afterwards the fine earth fraction (<2 mm) was analyzed for bulk mineral composition using X-ray diffraction (Siemens D500, Cu Kalpha radiation, powder mounds) and Rietveld software. Geo-chemical composition was determined with a Siemens SRS 200 X-ray fluorescence apparatus (Cr radiation). Free iron was measured by an adapted DCB extraction (12 h, room temperature). Finally, granulometry was assessed using a combined

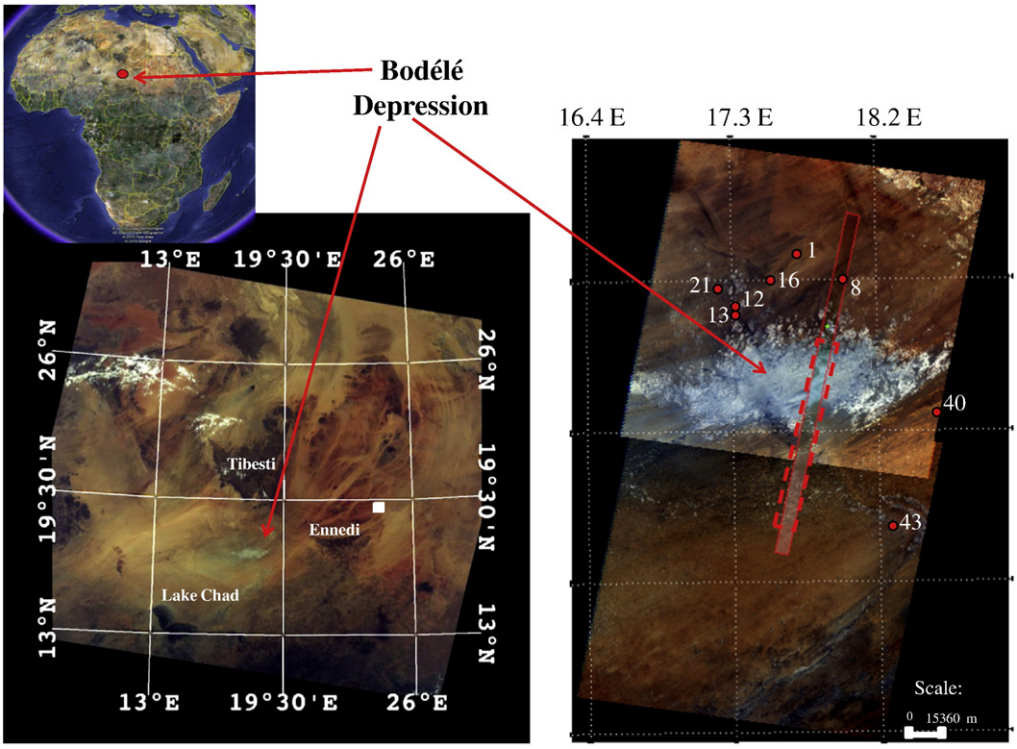

Fig. 1. Geographic setting: Hyperion satellite path pasted over the mosaic of two Landsat images. Also shown is the location of our reference field samples (Tables 1 and 2). Area demarcated by dashed lines is selected for the comparison between calm and stormy states. This figure shows the location of the calm image relatively to the upwind sources (relative to the sampling area).

Table 1
Surface description for reference sample sites.

Site	Depth	Stone content	Stone size	Slope gradient	Surface type	Surface color
	cm	%	cm	°		Munsell
1	−2	95	<4	1–2	Coarse serir	10YR7/6
8	−2	95	<2	2	Fine serir	10YR7/4
12	>30	0	–	<1	Lacustrine	2Y8/2
13	1	0	–	1	Lacustrine	2Y8/2
16	1	90	>1.5	1–2	Coarse serir	10YR7/4
21	1	95	>1.5	<1	Fine serir	7.5YR//4
40	1	85	<5	1–2	Middle serir	10YR7/4
43	>10	0	–	0	Basin	10YR8/1

sieve (sand) and pipette procedure (silt and clay) in water. These samples supplied reference for the Hyperion reflectance data. In particular, sample #8 (sandstone outcrop surface) is visible over the Hyperion image while others can supply additional benchmarks of the study area, see Figs. 1 and 2 and Tables 1 and 2.

3. Methodology overview

We examined two images over the Bodélé Depression (17° N, 18° E), Chad, acquired by Hyperion EO-1: (i) June 7, 2003 at 9:04 am local time during a dust storm event; (ii) June 21, 2003, at 9:06 am on a calm day.

Several strategies could be applied to analyze hyperspectral data. Band ratios provide an efficient way to emphasize subtle spectral variations at the surface (Clark & Roush, 1984). Linear Spectral Unmixing (LSU) has been specifically developed to account for mixtures (Adams et al., 1986) and can be defined as a procedure by which the measured spectrum of a pixel is decomposed into a collection of constituent spectra–or End Members (EM)–and a set of corresponding fractions (abundances) that indicate the proportion of each EM present in the pixel (e.g., Adams & Gillespie, 2006). This method requires a set of EM (library) spectra that could come either from laboratory spectra of samples, field measurements, or spectra collected from the image itself. Spectral Angle Mapper (SAM) is a physically-based spectral classification that matches pixels to EM spectra. The algorithm determines spectral similarity by calculating an angle between the spectra as members of a vector space whose dimensionality equals the number of bands. Classifications based on statistical analysis form another group of methods (e.g. G-mode classification, Principal Component Analyses, and minimum noise fraction transform (MNF)) which can be combined with the Pixel Purity Index (PPI) (Boardman et al., 1995; Green et al., 1988).

In the present study, we began with a part of a Hyperion calm scene, geographically identical to its stormy Hyperion counterpart (highlighted in Fig. 1 by dashed red lines, Section 3.4). We used SAM classification and six EMs as an input for classification, based on reference sample composition (Table 2). Comparison of a reference EM with the most similar pure image pixel was also used as a quality pre-processing assessment of a calm image. A comparison of calm and stormy images is a second main part of our study. Here we use LSU to explore the differences in mineralogical composition of two scenes.

3.1. Image processing

Both images (calm and stormy) were pre-processed and adjusted according to the Hyperion user guide (Barry, 2001). Both images were then processed to remove molecular and aerosol scattering attenuation via the ACORN atmospheric correction code (AIG, 2001). Spectral smoothing (averaging of several consecutive reflectance values around a nominal wavelength, segment size for averaging 3×3) was applied to every pixel in the image (Duckworth, 2004). Additional smoothing filter (segment size 3×3) was applied across our working region (2080–2380 nm). Finally, the images were geo-referenced for subsequent spatial change detection analysis (for more details see Chudnovsky et al., 2009).

3.2. Spectral library

In this study we try to identify suspended and transported minerals. Since natural minerals are almost always strongly mixed, the input library was made from laboratory spectra of pure minerals (EM). We use the "USGS Spectral Library for Minerals" database (packaged with hyperspectral image-processing ENVI software, http://www.ittvis.com/) as a spectral reference for analysis of the Hyperion data.

The Bodélé Depression contains predominantly lacustrine sediments. These consist of clastic sediments originating from the Tibesti, clay minerals precipitated from the lake water (as presently happening in the Lake Chad), and limnic organisms (i.e. diatoms) (Herrmann et al., 2010). Bulk mineral composition of dust samples (as assessed by XRD analyses), shows not only the low-lying lacustrine sources but also the whole assemblage of erodible surfaces of the area contributing to the mineral assemblage of transported dust (Herrmann et al., 2010). Dust samples originating from the Bodélé Depression (e.g. Herrmann et al., 2009; Moreno et al., 2006; Prospero et al., 2002) are rich in silica (quartz and diatoms) and aluminosilicates (smectite, kaolinit) and

Table 2
Reference samples their coordinates and physical, chemical and mineralogical properties.

Chad	Coordinates		Fe total	Fe d[a]	Sand	Silt	Clay	Bulk mineral composition
Sites	N	E	%	%	%	%	%	
1	178	1792	0.85	0.4	94	4	2	Quartz 94%, feldspars 5–15 and the rest mainly layer silicates
8	1777	1735	1.39	0.5	90	6	4	Quartz 90%, feldspars 5–15 and the rest mainly layer silicates
12	1745	1748	4.83	0.9	2	57	42	23% quartz, 26% feldspars, 15% kaolinite, 21% mica/illite and 5% 14 A layer silicates, gypsum 5%
13	1738	1751	4.31	1.1	3	62	35	24% quartz, 26% feldspars, 24% kaolinite, 21–24% mica/illite and 5% 14 A layer silicates and gypsum >5%
16	1768	1768	0.82	0.3	92	6	2	Quartz 92%, feldspars 5–15 and the rest mainly layer silicates
21	1763	1723	1.33	0.3	91	6	3	Quartz 91%, feldspars 5–15 and the rest mainly layer silicates
40	1691	1871	0.63	0.2	92	6	2	Quartz 92%, feldspars 5–15 and the rest mainly layer silicates
43	1624	1862	0.67	0.2	13	50	37	Calcite 28%, gypsum 2%, quartz 28%, feldspars 4%, kaolinite, 21%, mica/illite 12% and 5% 14 A layer silicates

[a] "free" iron as determined by cold dithionite extraction (12 h).

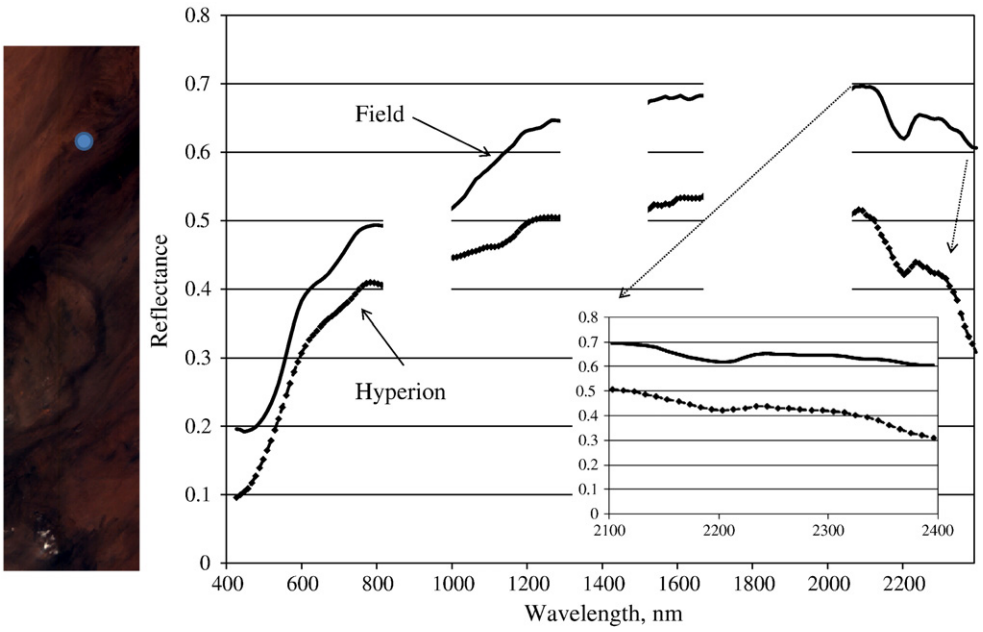

Fig. 2. Mineralogy validation for one reference sites. Upper panel: Zooming in on sample site 8: field spectrometer and Hyperion spectral measurements for the entire spectral range VIS-NIR-SWIR. Lower panel: Zooming across 2080–2380 nm.

silicates (feldspar), accompanied calcite. The mineral composition of the soil/sediment samples varies depending on the major genetical processes. Here only the uppermost soil/sediment samples are described. Granulometry has a strong impact on the mineral composition. Since serir surfaces are coarse in nature, quartz dominates, locally varied by Fe-oxyhydrates (from iron-rich sandstone). Feldspars (i.e. albite) as tectosilicates are also more prominent in the coarser size fractions. The lacustrine samples with a silty to clayey texture are relatively rich in phyllosilicates, mainly Mg- and/or Fe-rich smectite (see also Gac et al., 1977; Pedro et al., 1978). Also kaolinite and illite occur but in different shares. Only lacustrine samples have shown significant presence of gypsum, depending on the evaporitic nature of this sediment type (Herrmann et al., 2010).

Literature review (Bristow et al., 2009; Castillo et al., 2008; Chappell et al., 2008; Moreno et al., 2006; Mounkaila et al., 2003; Prospero et al., 2002; Wright, 1985) and our field analyses yielded an approximate database library consisting of 18 minerals that can be found in the study area: phyllosilicates (muscovite, illite, vermiculite, montmorrillonite, nontronite, saponite, chlorite, kaolinite, and palygorskite), oxides and oxihydrates (gibbsite, hematite and goethite), sulfates (gypsum) carbonates (calcite, dolomite), and other silicates (albite and pargasite) including quartz. Quartz, hematite, goethite, albite, and pargasite were excluded from the overall analyses because they lack absorbance features across the long wavelengths. This left 12 minerals as input for mixture analyses. While being somewhat restrictive, when compared to the true mineral diversity in the study area, this database nevertheless captures the essential signatures as shown below.

3.3. Calm scene analyses

Based on field analyses of the likely minerals on the ground (Table 2), pixels that best matched the spectral signatures of six endemic minerals were identified via the SAM classifier (Boardman, 1998). Since no validation of a dust storm image is possible, one resorts to the calm scene analyses for an additional assessment of the quality of dust image spectra. The following reference minerals were used: illite, vermiculite, montmorollonite (smectite), nontronite (Fe-rich clay), kaolinite, and calcite. We extracted the spectral signatures of these minerals from the USGS spectral library (e.g. reference spectra, or EM), and applied SAM classifier to the calm scene of the Hyperion image data in order to locate the pixels with spectral signatures closest to data base minerals. SAM classifier treats an observed reflectance spectrum as a vector in a multidimensional space, whose number of dimensions equals the number of spectral bands (Lillesand & Kiefer, 2004). To compare image pixel spectrum and a library EM spectrum, SAM technique defines the multidimensional vectors for each spectra and the angle θ between the two vectors is calculated (Kruse et al., 1993). If this angle is smaller than a given tolerance level, the spectra are considered to match (e.g. the closer the resemblance to the reference spectrum). Pixels exceeding angle threshold θ_{MAX} are identified as not belonging to the class of materials identified by the reference EM. We used a threshold of $\theta_{MAX} = 0.1$ radians (Kruse et al., 1993) to find pixels, spectrally similar to the reference USGS spectrum (see Fig. 3b). Average spectra of the selected pixels were then compared to the reference EM spectrum. Next, the pixels, spectrally closest to each of the reference minerals were overlaid on a calm scene to show the distribution of the spectrally predominant minerals (based solely on absorption features). Because of relying on spectral shapes (as opposed to overall magnitude), SAM is less affected by the variable contribution of the illumination (or albedo) and topography across the scene (Lillesand & Kiefer, 2004).

3.4. Calm vs. stormy scenes

How should one best compare calm and stormy images? We employ the following approach to account for the EM spectra. First we apply the LSU, where the observed spectral response from an area on the ground is assumed to be a linear mixture of the individual spectral signatures of the various surface cover types (in our case, minerals). Next, we determine spectral changes of a given pixel from calm to stormy conditions in order to enable a spatial view of the differences and abundances of the selected EMs. LSU may also shed light on mineral variability between both images. In LSU, the weight for any given EM signature is the fractional area occupied by the associated mineral. LSU approach used in this study is designed to match an unknown spectrum (a mixture) using a linear combination of reference EM spectra. Each pixel of an image is processed independently (Boardman, 1989, 1993; Lillesand & Kiefer, 2004). Based on our

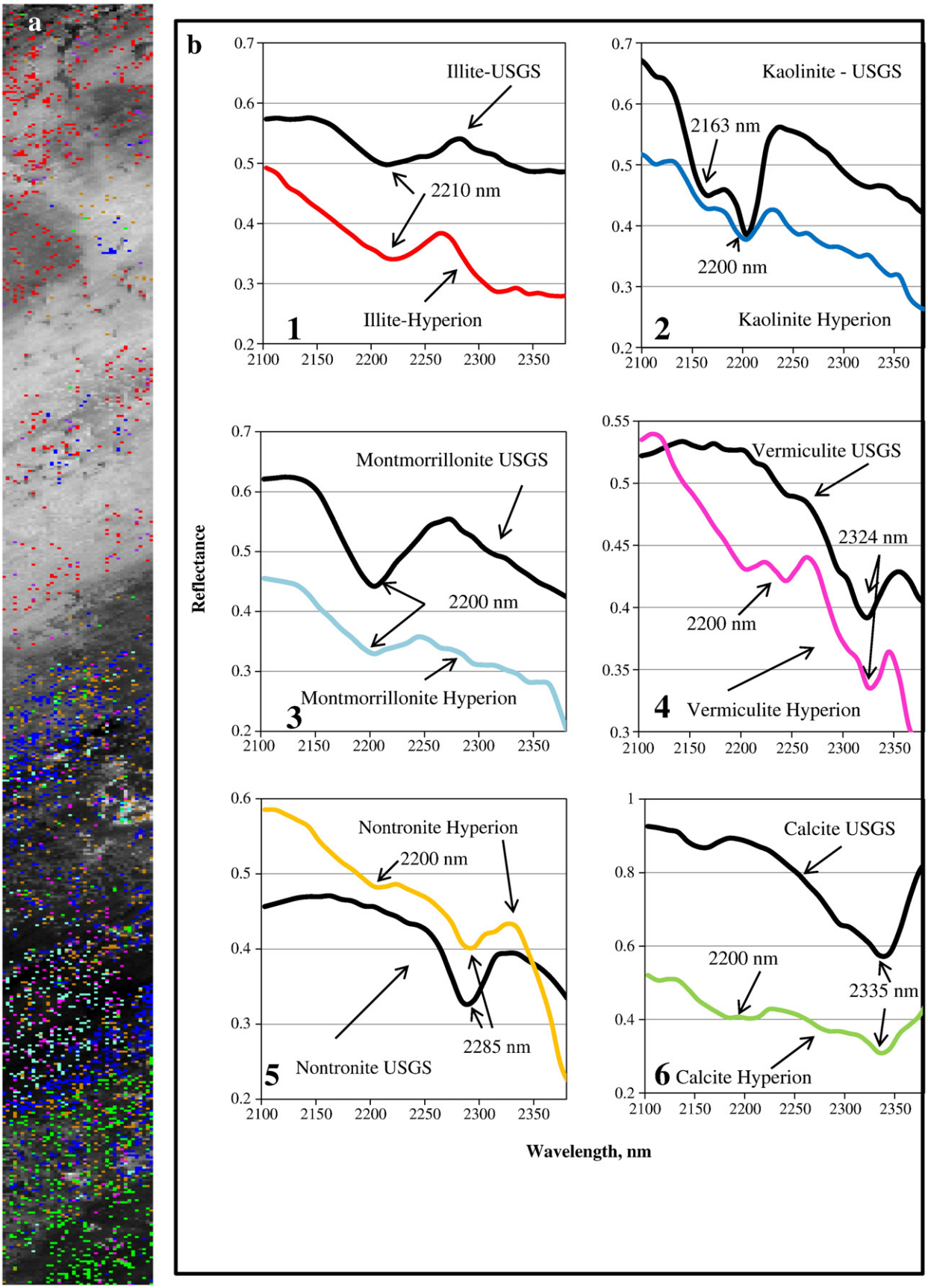

Fig. 3. Mineralogical composition map of the calm image. Left panel: distribution of six main minerals within the image. Spectral signatures of the minerals used to identify the image pixels most closely matched to the spectral library signatures, and thus chosen to represent locations where that mineral is dominant. Right panel: Mean reflectance spectra of the corresponding pixels (color), compared to the spectral library signatures for the basis minerals (black).

reference spectral library, all the n = 4 combinations of EMs for both images were explored. This way we identified the minerals shared by both images. Solutions with negative coefficients were discarded and one with the lowest Root Mean Square Error (RMSE) was retained. The maximum number n = 4 of EM used in LSU analyses was selected because it allows about 90% of the pixels of an Hyperion image to be modeled with RMSE lower than 35%. We observed, that setting gypsum as additional EM (n = 5) reduced the RMSE to 25% while setting n = 3 decreased dramatically the quality of the results. Importantly, LSU analyses performed by using smectite and illite as a separate EM in the input library gave higher RMSE values for stormy pixels. Probably, nearly equal absorption wavelengths for smectite and illite (i.e. 2200 vs. 2210 nm) cause such errors. This confirms the initial choice of grouping these minerals in a single spectral family in order to avoid over-interpretation within a family of clays (phyllosillicate group of minerals).

Finally, we analyzed the RMS pixels to determine areas of missing or incorrectly selected EMs. Higher RMSE values suggested an incomplete EM selection for the corresponding pixels or other causes of bias between the linear assumption of the LSU and the true spectra of suspended dust. Lower RMS values demonstrated successful mineral identification for the pixel in question.

In order to contrast the dust plume and the underlying surface, and to quantify the change between stormy and calm scenes, we calculated a Spectral Ratio Images (SRI) for each wavelength: stormy/calm. A major advantage of using SRI is that it conveys the spectral or color characteristics of image features, regardless of variations in scene illumination conditions (Lillesand & Kiefer, 2004). In addition, the SRI shows calm to stormy changes in slopes of the spectral reflectance, regardless of the absolute reflectance values. We scaled the SRI results by using area with no apparent spectral changes. The expected SRI for "no-change" is unity in all of the spectral bands, was used as EM. If the average deviation from the EM "no change" spectrum at all wavelengths falls within values of ±0.10–0.12, the image spectrum for that pixel is considered to match the EM. Next, SRI image was used as a base image for SAM classification. Our previously defined "no-change" EM was selected as input. Here SAM was applied separately for visible (400–680 nm) and for 2080–2380 nm. We used a threshold of $\theta_{MAX} = 0.1$ radians (Kruse et al., 1993) to find pixels, spectrally similar to the EM. Pixels further away than a specified maximum angle threshold θ_{MAX} were identified as areas of apparent change between two scenes, whereas the opposite was defined for the areas where no spectral change had occurred.

4. Results and discussion

4.1. Laboratory vs. remote hyperspectral data

Mineral compositions of field samples are quite similar and include quartz, feldspars, mica/illite, vermiculite, kaolinite, and gypsum (Table 2). The clay mineral composition of the clay fraction (<2 μm) as determined by semi-quantitative analysis on sediment specimen in samples #1, 8, 16, 21 and 40 comprises smectite (40–65%), kaolinite (10–40%), vermiculite (5–30%) and illite (less than 5%). Based on the geo-chemical data and on texture and bulk mineralogy, we conclude that a significant fraction of Fe is bound in the phyllosilicates (mainly clay minerals). Fig. 2 shows the reflectance spectra of sample #8 (serir surface with sandstone fragments) measured by an IRIS spectrometer vs. Hyperion spectra showing the whole spectral range (400–2400 nm). As shown in Fig. 2, Hyperion data and the real surface reflectance spectra are similar. Both curves exhibit absorption (dips in reflectance) around 650 nm (Fe-oxides) and at 2200 nm (clay minerals). Sample #8 appears as yellowish brown (10YR7/4 dry Munsell color) and across visible region exhibits absorption at 650 nm due to free iron compounds. By exploring image pixels from North to South it was observed that the dip at 650 nm is more pronounced for sample #8 and areas north of Bodélé on Fe-rich sandstone, and weaker for the cover sands towards the southern part of the image.

4.2. Surface mineralogy

What are the dominant minerals found in and around the Bodélé Depression? Fig. 3 highlights similarities between the spectral signatures of the image and the USGS spectral library. Fig. 3a shows the SAM distribution of six reference minerals above calm Hyperion grey-coded image at 586 nm. In Fig. 3b, for each mineral, the mean reflectance spectrum of the corresponding classified pixels (same color) is compared to the spectral library signature for that mineral (shown in black). These results confirm the appearance of the reference EM minerals. It also shows important spectral differences among the minerals, in terms of size, shape, magnitude and wavelength position of absorption features.

All sites (including all petrographies) show a broad absorption centered at 2200 nm representing aluminosilicate clay minerals (illite, kaolinite, and montmorrillonite). There is a hint of some carbonates in the southern areas. The measured spectra indicate these and other minerals, with overlapping spectral absorption features (Fig. 3b, panels 1–6). Kaolinite can be separated from illite and smectites because of prominent doublet absorption at 2163 nm and 2200 nm. Fe- and Mg-rich smectites are also found throughout the area (Herrmann et al., 2009; Mounkaila, 2006) as, indeed, indicated by absorbance by Fe/Mg hydroxyl bonds around 2300 nm: (Hunt, 1977). High Fe concentrations found in lacustrine sediments (Table 2) are related to local sedimentary conditions. Throughout diatomite and lacustrine sediments we observe the spectral features of nontronite at 2285 nm — a Fe-rich clay mineral as expected in and around the Bodélé, based on Mounkaila (2006). Pedro et al. (1978) raised the question of nontronite origin in Lake Chad lacustrine sediments. These authors observed the formation of nontronite by combination of previously precipitated ferric hydroxides with silica (or silicate minerals), under slightly reducing conditions.

Sand dunes and areas from the southern part of the image show absorption near 2335 nm, indicating carbonate (calcite) presence but field data to confirm this is not yet available. Gypsum (sulfate group) is also detected in lacustrine sediments but it lacks unique absorption bands across the 2080–2380 nm. Field samples (Table 2, samples 12, 13), however, confirm the presence of gypsum in lacustrine sediments. In addition, we also rely on the convexity in the curve between 2330 and 2350 nm to indicate the presence of gypsum (Chudnovsky et al., 2009). Finally Mounkaila (2006) detected 6.6% of gypsum in sample 43 located in the southern part of the image in Fig. 1.

The relevance of the LSU modeling results can also be checked by looking at the spectral adjustment. Fig. 4 shows a comparison between the data (thick line) and the linear mixing model (dotted-dashed lines) for two pixels in kaolinite-rich and vermiculite-rich areas, respectively. Dashed and dashed-dotted lines correspond to spectra of EM which have been retained by the LSU, multiplied by their mixing coefficient. It shows how much a given EM contributes to the final modeled spectrum. The presence of several diagnostic bands such as kaolinite, vermiculite and Fe-rich clay (nontronite) improves the confidence level in the detection of the corresponding mineral.

4.3. Lifting of dust

Here we explore the differences in mineralogical composition between calm and stormy images as a step towards understanding of the dust lifting process. In addition, we study the influence of the underlying background on the monitoring of atmospheric dust. Fig. 5c–g shows the LSU output where calm and stormy images pixels were used to determine the fractional cover of kaolinite, illite–smectite, Fe- and Mg rich clay, and vermiculite. Both images exhibit spatial heterogeneity in the fractional cover of minerals. Moreover, for

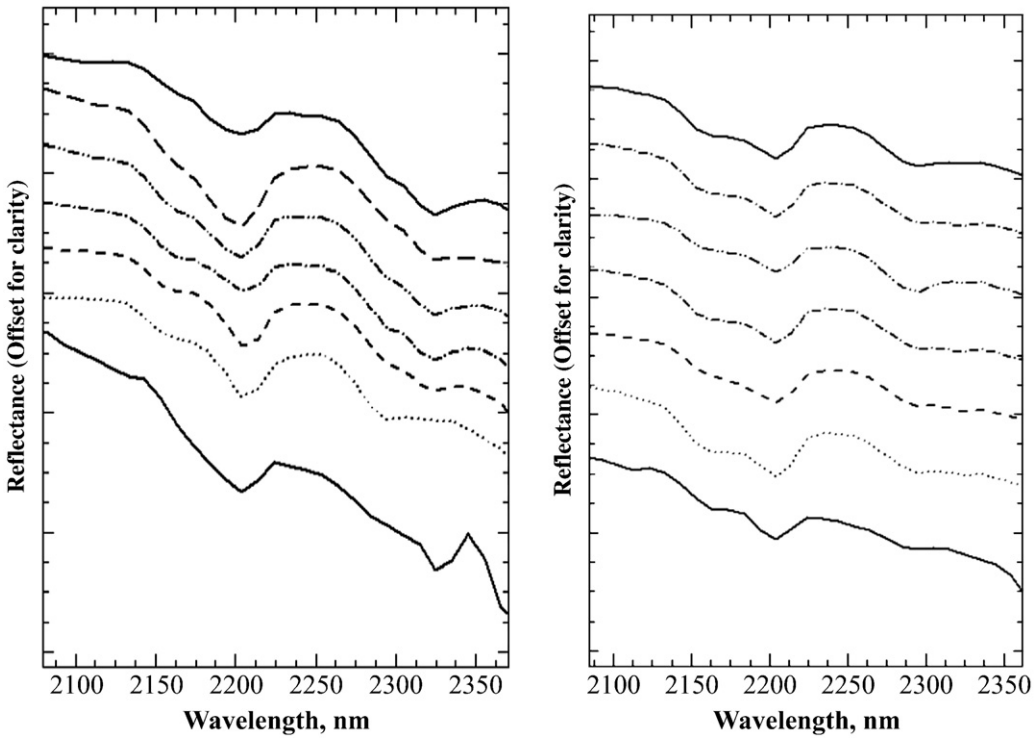

Fig. 4. Comparison between Hyperion data (denoted as 1) and spectral mixture model. Each spectrum of the input library (vermiculite, kaolinite, illite, and nontronite) has been multiplied by its mixing coefficient. Left: (2) 20% vermiculite, 20% nontronite, 30% kaolinite, 30% illite; (3) 40% vermiculite, 10% nontronite, 20% illite, 30% kaolinite, (4) 50% vermiculite, 10% nontronite, 10% nontronite, 20% illite, 20% kaolinite, (5) 50% vermiculite, 10% nontronite, 20% illite, 20% kaolinite; (6) 40% vermiculite, 10% nontronite, 20% kaolinite + 30% illite; (7) 60% vermiculite, 10% nontronite, 20% illite, 10% kaolinite. Mixture 7 was found to be the best matched spectra with the lowest error comparing to others. Right: (2) 10% vermiculite + 10% illite + 30% kaolinite + 50% nontronite; (3) 10% illite + 10% vermiculite + 50% kaolinite + 30% nontronite; (4) 20% illite, 20% vermiculite, 50% kaolinite, 30% nontronite; (5) 10% ver + 10% illite + 30% kaolinite + 50% nontronite; (6) 10% illite + 20% vermiculite + 40% kaolinite + 30% nontronite; (7) 10% vermiculite + 10% illite + 30% kaolinite + 50% nontronite; (8) 10% illite + 10% vermiculite + 40% kaolinite + 40% nontronite. Mixture 6 has the lowest error.

the stormy state, most minerals exhibit a change in per-pixel fractions towards southern part of the image. Vermiculite fraction does not exhibit such a change. Possible explanations for these differences include: 1) transport mechanism process favoring finer sizes and therefore clay minerals (Herrmann et al., 2009); 2) different mineral assemblage of dust from upwind sources in comparison to the surface material (Herrmann et al., 2009); 3) difference in spectral contrast between dust and its underlined bright/dark surface. In fact, visual interpretation of other Landsat images from stormy days has shown that lacustrine surfaces are strong emitters if conditions are matched

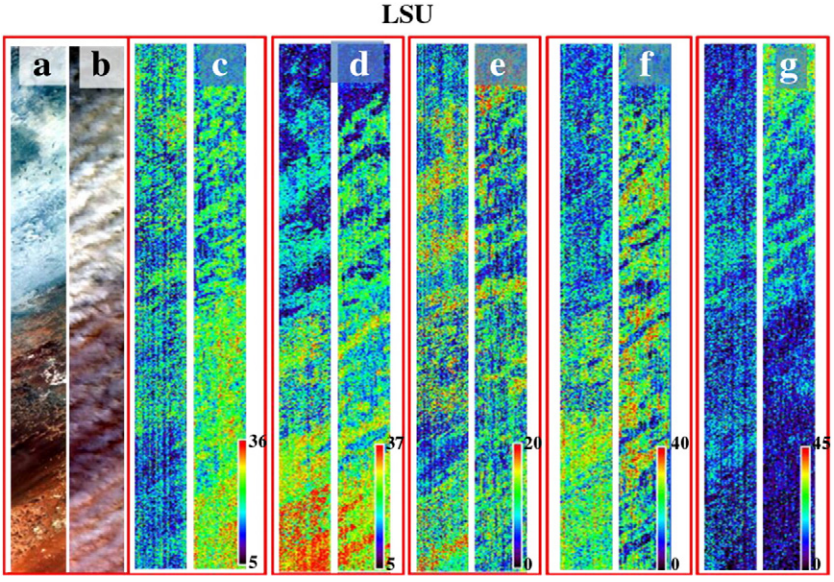

Fig. 5. Anatomy of a dust storm revealed by mineral tracers. LSU results for the calm day image (a, natural color) and the dust storm image (b, natural color). Color-coded are per-pixel fractions of five basis minerals: c: kaolinite, d-illite-smectite, e-Fe-Mg rich clay, f- vermiculite, and g- RMS error (%). The LSU results agree with our field study (Table 2) and with earlier image analysis (Chudnovsky et al., 2009). Insofar as the classification reveals surface morphology (contours), storm anatomy is revealed as well, unless completely obscured by scattering. The mineral fractions provide striking markers of spatial tongue-like structures, embedded within the north-easterly dust plumes, advected by the prevailing winds between two mountain ridges.

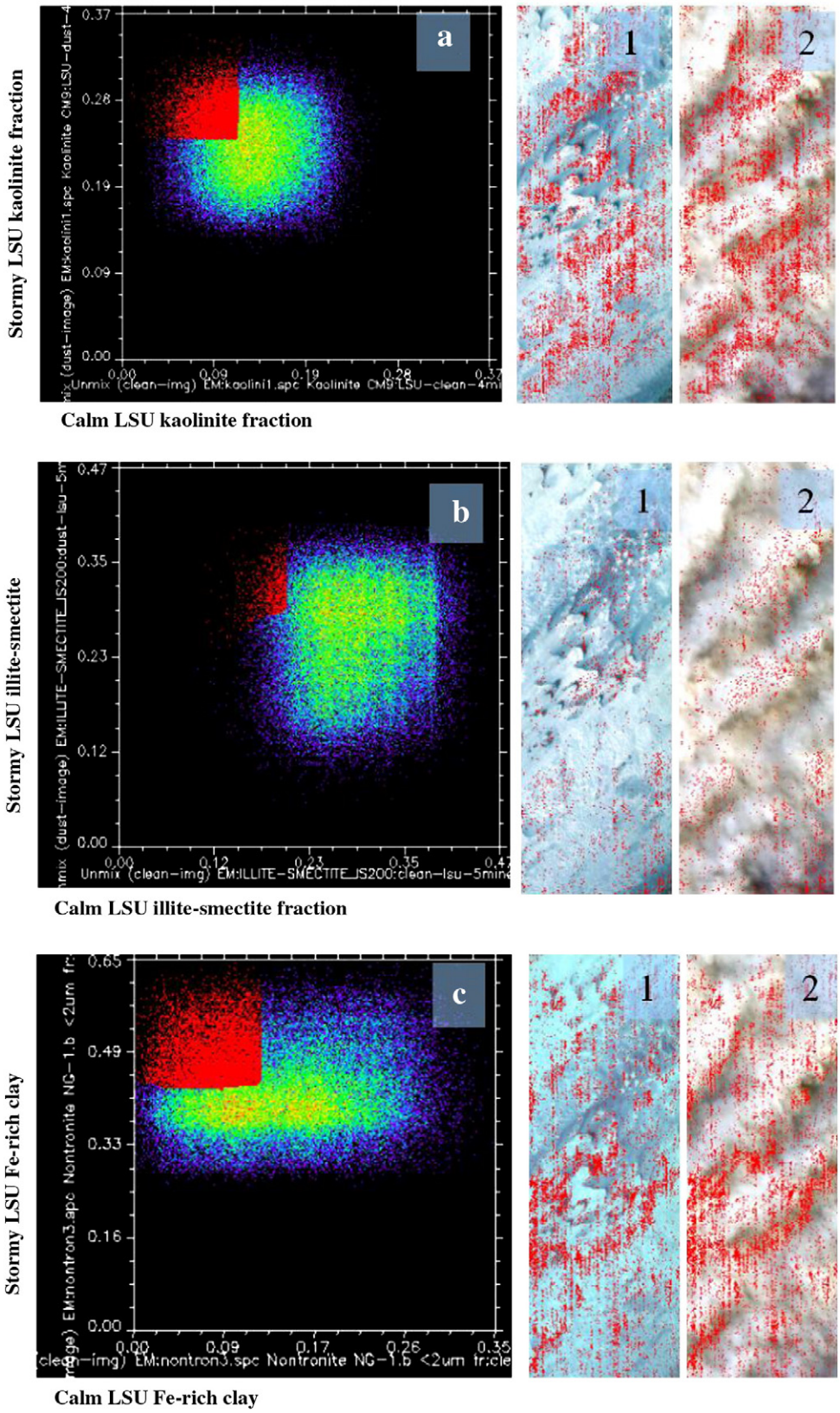

Fig. 6. Scatter plot of calm vs. stormy LSU classification shown as mineral contrast in both conditions. Left (a and b): Pixel per-pixel kaolinite fraction (a, upper) of a stormy state plotted vs. the same fraction in a calm state. Numerical ranges of these fractions barely overlap, indicating upstream origin of stormy kaolinite. Highlighted in red are pixels with low kaolinite content in the calm state image *and* high kaolinite content in stormy state. Right: "Red pixels" are overlaid on RGB of calm (1), and stormy day (2). Illite–smectite and Fe–Mg rich clay fractions for both states are presented in panels b and c, respectively. Remarkably, these pixels are faithful flow tracers. This is evidenced by the wavy jet-like morphology of the red pixels (kaolinite-deficient in clean state), whose axes are aligned with the north-easterly winds.

(presence of saltating particles). Thus explanations 2 and 3 are most probable. The difference between the northern and southern part of the image is that in the northern particles entrained from the lacustrine surfaces are traveling over lacustrine surfaces, while in the southern part after entrainment from the spotlike occurring lacustrine surfaces, the material is traveling already after short distances over different surface types. The grain size distribution and grain size selective dust uplifting at the study area require separate research and laboratory analyses (see Maurer et al., 2010).

LSU analyses show that the abundance of studied minerals for both states varies across the image. So, which pixel states (stormy or calm) show higher phyllosilicate mineral fractions? What are the differences per pixel with respect to clay composition? A scatter plot comparing the LSU quantitative mapping of each mineral pixel for stormy and the calm image state is an effective way to explore this. Random scatter suggests no correlation of LSU results between the two states and indicates that significant changes during the storm event whereas the opposite is implied by a linear scatter plot. Scatter plots for kaolinite, illite–smectite and Fe–Mg rich clay (Fig. 6) show random scatter type. This result reflects the influence of upwind sources on the LSU output for the stormy state. For example, the scatter plot for kaolinite (Fig. 6, upper left) shows that calm pixels may have <10% of kaolinite, whereas the same pixels in the stormy state show >25%. This is explained by the fact that terrestrial sources with higher kaolinite share contribute to the signal to the generally kaolinite poorer lake sediments, where kaolinite was diluted by precipitation of 2:1 phyllosilicates from the evaporating lake water. Generally, the center of the scatter plot is shifted to the left of the 1/1 line, representing a trend toward higher kaolinite concentrations during the storm event and suggesting downwind transport.

We highlighted in red all pixels with large calm to stormy differences (Fig. 6-1 and -2). Strikingly, the red pixel geometric pattern matches up with the predominant northeasterly wind direction characteristic for Harmatan condition in West Africa and reinforced locally by the orographic obstacles Tibesti and Ennedi. The long fetch is conducive to the Owen effect (Gillette, 1999). The fact that kaolinite and illite–smectite fractions show a different pattern might be related to the differences in average grain size. While kaolinite can grow under terrestrial conditions to sizes >2 μm, freshly precipitated smectite often occurs in the submicron range. Thus kaolinite frequency is higher where the dust plume is less thick (less bright on the image) meaning a transport closer to the surface.

Thus, LSU analyses and scatter plot comparison of calm and stormy images reveal the morphology of a dust storm (Figs. 5, 6). In particular, abundances of all studied mineral components reveal flames/"tongues", aligned with prevailing wind patterns (NE). Why are these "flames" so consistent in direction? Local topography promotes strong NE winds via funneling by the Tibesti and Ennedi mountain ridges (Washington & Todd, 2005). The NE propagation pattern emerging from our analyses points towards a long-term process confirmed by similar pattern (i.e. Herrmann et al., 2009) and frequent NE-oriented landscape features on the respective Landsat images (see Fig. 1). It also points towards homogenization of the fine fraction over large areas via constant redistribution of surface material, especially its finer fractions as already stated by Herrmann (1996). Furthermore, as evident from LSU analyses, these "flames" cover different types of the underlying surface (Figs. 5, 6) such as barchan-type dunes, obscured by the dust plume.

RMSE images shed additional light on the minerals missed in our classification scheme. From Fig. 5g, the pixels with the largest error for the stormy case were selected. These pixels suggest the presence of minerals not included in our analyses. In Fig. 7(a), we compare the high RMSE mean spectral reflectance curve (taken from the stormy image pixels) (denoted as 1) with spectral reflectance of several other diatomite surfaces: sample #12 (lacustrine sediment surface north of Bodélé Depression) measured by IRIS spectrometer (denoted as 2),

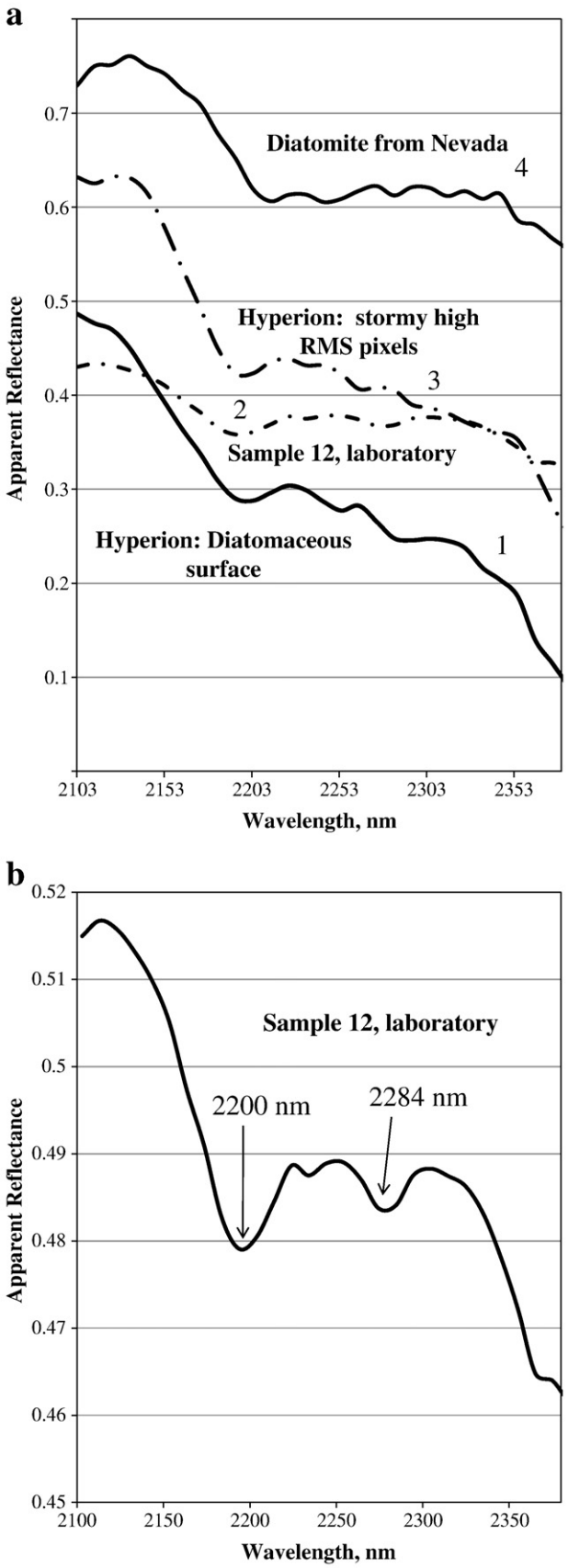

Fig. 7. Spectrum comparison. a: Mean spectra of high RMS values compared with diatomite surface as measured by Hyperion, by field spectrometer (sample #12, Fig. 1), and diatomite collected in Nevada, USA. b: Zoom in on sample #12 showing pronounced absorption features across 2080–2380 nm. Note absorption at 2200 nm related to clay minerals and at 2284 nm related to Fe–Mg–OH group.

surface denoted as 3 which is spectrally similar to sample #12 but measured by Hyperion, and surface 4, other kind of diatomite from Nevada, USA (Kratt et al., 2006). In order to get spectra of surface 3, spectra of sample #12 was used EM for SAM classification, and pixels most spectrally similar to #12 were therefore selected. This was done since sample #12 is not within the Hyperion path and no image spectra for this sample can be provided except of looking for spectrally similar pixels. Reference sample #12 is pure finely sized bright lacustrine sediment (Tables 1, 2), characterized by high Al and Fe content, low kaolinite, and high smectite (60% in clay fraction) concentrations (Herrmann et al., 2009). Note that this sample represents a lacustrine environment with reducing, neutral to slightly alkaline (Mg-rich smectite, gypsum) conditions. The diatomite spectra appear similar to the spectra of high RMS pixels. Hence, suspended dust may also contain diatomite tracers. This is to be expected since several authors (i.e. Drees et al., 1993; Mounkaila, 2006) described diatom occurrence in Harmattan dust samples collected over eastern West Africa. However, low spectral contrast precludes quantitative estimates of atmospheric diatomite particle concentration above an underlying diatomite surface. And even over non-diatomite surfaces non-crystallinity and transparency of the material hampers quantification. Therefore, this surface was excluded from the LSU analyses due to the lack of pronounced absorption features across SWIR. Larger errors are also observed in the northern part of the image, where the surface is dominated by a mixture of sand and diatomite and the dust plume is less dense. Note that diatomite from Nevada is different in its mineralogical properties (Kratt et al., 2006).

It is equally important to note that variations in mixing coefficients account for both mineral fractions and particle size. Thus, minerals contained in a surface do not contribute to the total reflectance spectrum as a sum of reflectance spectra, and the coefficients obtained for each mineral are not equal to their true abundance (e.g. unlinear mixing, Hapke, 1981, 1993). As a consequence, this method can be used as a qualitative detection of components only. Here, for a given mineral we establish calm to stormy variation maps and interpret these as relative spatial distributions. This allows for quantitative comparison and dust storm monitoring.

In order to quantify the relative change between stormy and calm scenes, the SRI image is displayed in Fig. 8(c–d) across 400–680 nm and 2080–2380 nm. As can be seen, sands located at the northern part of the image (denoted by 1) appear in darker tones, indicating no significant changes between the two dates. This is probably due to several facts: i. the occurrence of serir surfaces hindering deflation and ii. the wind shading due to the closer setting to orographic highs. Higher ratio values are depicted in brighter tones. Across 400–680 nm, the main change occurs above sands (southern part of the image) caused by the floating dust increasing the overall albedo over the relative darker terrestrial materials; whereas for 2080–2380 nm, brighter tones appear above bright lacustrine sediments and sands (central and southern parts) caused by the mixed transported material increasing i.e. the kaolinite signal over lacustrine surfaces and decreasing it over terrestrial ones. The SAM classifier based on SRI for 400–680 nm and 2080–2380 nm, respectively is displayed in Fig. 8(e–f). Across 400–680 nm, the areas of change appear above sands (red colored tones), where the spectral contrast above underlying surface and the dust plume is the highest across the image. In contrast, when SAM is applied across 2080–2380 nm, the main change is centered above bright lacustrine sediments and sandstone outcrops. These results lead us to the conclusion that 2080–2380 nm has a potential to retrieve the dust plume signature by tracing clay minerals over the bright surfaces.

5. Concluding remarks

We've argued that spaceborne hyperspectral sensors can detect differences in mineralogical composition of calm and stormy images,

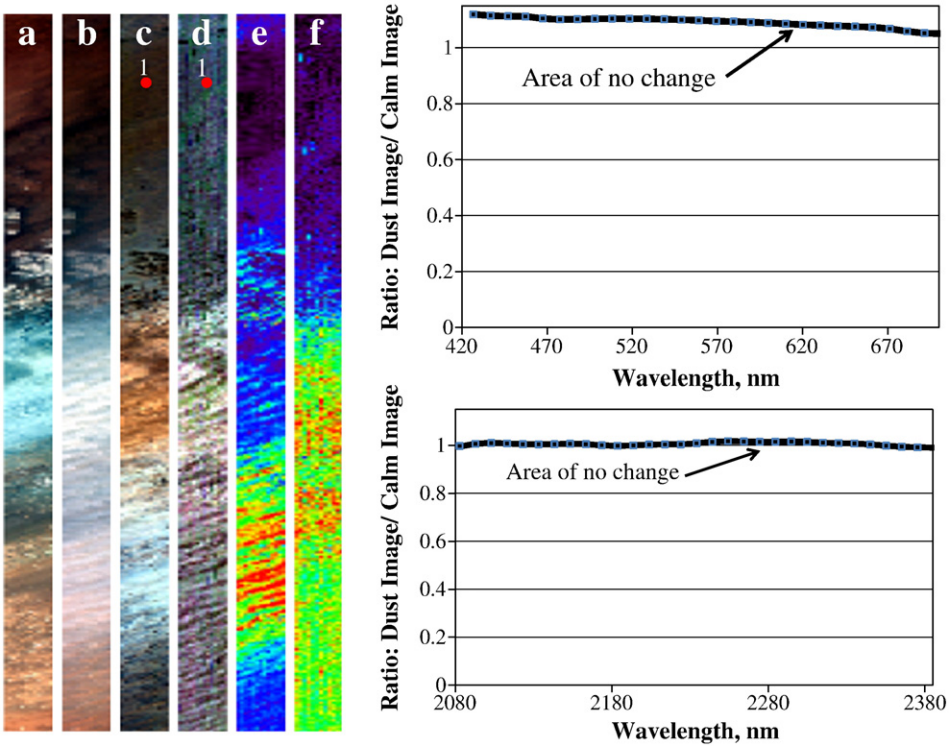

Fig. 8. Relative stormy to calm changes. (a, b) Color composites of Hyperion data for the Bodélé obtained on June 7, 2003 (calm day) and June 21, 2003 (stormy) (c,d, respectively). Color composites of Ratio Image (stormy/calm) in VIS and SWIR, respectively. For (c) 640 nm is displayed as red, 548 nm as green and 457 nm as blue (RGB, bands 22, 13 and 5 respectively). For (d) 2300 nm as red, 2200 nm as green and 2100 nm as blue (bands 155, 145 and 135). (e–f) SAM classifier based on SRI for 400–670 nm and 2080–2380 nm respectively. Darker (blue) tones indicate regions of insignificant changes between the two dates. (g) The spectral reflectance of area 1, representative of insignificant spectral change (hence, the ratio values are about unity).

thereby contributing to our understanding of dust lifting patterns. We also examined the weak contrast problem occurring in the vicinity of a dust source, rendering difficult the separation of a dust plume from an underlying surface. To that end, we identified the main minerals presented at the surface of the calm state image using SAM classifier. Next, we applied LSU on a pixel-by-pixel basis to determine mineral fractions that calm and stormy images share. The lowest RMSE was retained for kaolinite, illite–smectite, Fe-rich clay (nontronite) and vermiculite. These fraction assessments of each mineral for both images enabled us to track dust plumes. Minerals, lifted and suspended particles downwind of a dust source were thus identified.

The calm vs. stormy classification technique was also applied to the Ratio Image with the aim to study the dust signature and the calm vs. storm mineral contrast. Importantly, across 2080–2380 nm, the contrast above bright areas is discernible. Although, for certain minerals this contrast might be low and morphological rather than spectral in character, the spatial dissimilarity between the two states is rendered evident.

The results reveal the tongue-like formations in the stormy state, indicating suspended dust entrainment by NE winds. The dust signature is characterized by a clay mineral assemblage (kaolinite, illite-moscovite, and Fe-rich nontronite) mixed, presumably, with eroding diatomites. Our analyses rest on pronounced spectral absorptions across SWIR with features centered at 2200 nm, 2285 nm, 2300 nm and 2324 nm (metal (Al–Fe–Mg)–OH absorptions). These lead us to the conclusion that clay minerals may be used as tracers for atmospheric dust monitoring even above bright areas. Future missions should explore the possibility of retrieving aerosol optical depth (AOD) over bright areas based on 2080–2380 nm, with high spectral resolution capabilities. Such information cannot be obtained from current generation of satellites in orbit, such as MODIS.

There is much to explore, as our analysis of dust mineralogy is not complete. The atmospheric scattering in the visible region is more complex than in the shortwave and requires a more complex modeling than simple weighting. Also, spectrally featureless minerals within 2080–2380 nm e.g., quartz and feldspars have not been considered. Of course, minerals with similar absorption such as vermiculite and chlorite (both at 2324 nm) cannot be separated. We also plan to explore the thermal region (see http://www.enmap.org/ and http://hyspiri.jpl.nasa.gov/).

Despite the limitations, our approach demonstrates considerable potential of hyperspectral data for dust mineralogy and transport. In particular, hyperspectral monitoring of dust plumes over dark background downwind of the Bodélé dust source such as over Lake Chad should be done. Here background is less pronounced so that quantitative and mineral analyses will likely be more precise. Propagation pattern analysis towards identification of other “hot spots” (prolific dust emitters) is also of great interest but the narrow Hyperion path does not cover these regions. Another issue is localization of iron sources. Chudnovsky et al. (2009) pinpointed the presence of goethite in topsoils of the Hyperion image. However, field samples show high total Fe concentration of lacustrine sediments (grey-bright surfaces). How is the iron bound in these sediments and how does it contribute to the long-range transport? This affects fertilization of the Amazon Rain Forest as well as the oceanic phytoplankton.

Acknowledgements

Authors greatly appreciate Dr. Mounkaila M. important comments. A. Chudnovsky is grateful to the Dept. of Physics of the Michigan Tech for their hospitality and support. Deepest thanks are given to the Head of the Department, Prof. Ravi Pandey and to the secretary Kathy Wollan. A. Chudnovsky is grateful to Prof. Petros Koutrakis from Harvard School of Public Health for his support. The authors also greatly appreciate Mr. Guy Shwartz from Tel-Aviv RS Lab for programming using IDL. This work was supported in part by the US National Science Foundation through ATM05-54670.

References

Adams, J., & Gillespie, A. (2006). *Remote sensing of landscapes with spectral images. A physical modelling approach*. Cambridge, UK: Cambridge University Press.

Adams, J. B., Smith, M. O., & Johnson, P. E. (1986). Spectral mixture modeling: A new analysis of rock and soil types at the Viking Lander site. *Journal Geophysical Research, 91*, 8098–8112. doi:10.1029/JB091iB08p08098

Analytical Imaging and Geophysics LLC (AIG) (2001). *ACORN user's guide, stand alone version.* Analytical Imaging and Geophysics LLC. 64 pp.

Barry, P. (2001). *EO-1/Hyperion Science data user's guide.* Redondo Beach, CA: TRW Space, Defense & Information System.

Boardman, J. (1989). Inversion of Imaging Spectrometer Data using Singular Value Decomposition. Proceedings, IGARRS ‘89. *Twelfth Canadian Symposium on Remote Sensing*, *4*, 2069−2072.

Boardman, J. (1998). Leveraging the high dimensionality of AVIRIS data for improved sub-pixel target unmixing and rejection of false positives: mixture tuned matched filtering. *Summaries of the Seventh Annual JPL Airborne Geoscience Workshop, Pasadena, CA,* p. 55.

Boardman, J., Kruse, F., & Green, R. (1995). Mapping Target Signatures via Pixel Unmixing of AVIRIS Data. *Summaries of the Fifth Annual JPL Airborne Earth Science Workshop, JPL Publication 95–1*, *1*, 23−26.

Bristow, C., Drake, N., & Armitage, S. (2009). Deflation in the dustiest place on Earth: The Bodélé Depression, Chad. *Geomorphology*, *105*(1–2), 50−58.

Castillo, S., Moreno, T., Querol, X., Alastuey, A., Cuevas, E., Herrmann, L., et al. (2008). Trace element variation in size fractionated African desert dusts. *Journal of Arid Environment*, *72*, 1034−1045.

Chappell, A., Warren, A., O'Donoghue, A., Robinson, A., Thomas, C., & Bristow, C. (2008). The implications for dust emission modeling of spatial and vertical variations in horizontal dust flux and particle size in the Bodélé Depression, Northern Chad. *Journal of Geophysical Research*, *113*, D04214. doi:10.1029/2007JD009032

Chudnovsky, A., Ben-Dor, E., Kostinski, A. B., & Koren, I. (2009). Mineral content analysis of atmospheric dust using hyperspectral information from space. *Geophysical Research Letters*, *36*, L15811. doi:10.1029/2009GL037922

Claquin, T., Schulz, M., & Balkanski, Y. J. (1999). Modeling the mineralogy of atmospheric dust sources. *Journal of Geophysical Research*, *104*(D18), 22,243−22,256. doi:10.1029/1999JD900416

Clark, R. N., & Roush, T. L. (1984). Reflectance spectroscopy: Quantitative analysis techniques for remote sensing applications. *Journal of Geophysical Research*, *89*, 6329−6340.

Drake, N., & Bristow, C. (2006). Shorelines in the Sahara: Geomorphological evidence for an enhanced monsoon from palaeolake Megachad. *Holocene*, *16*, 901−911.

Drees, L. R., Manu, A., & Wilding, L. P. (1993). Characteristics of aeolian dusts in Niger, West Africa. *Geoderma*, *59*, 213−233.

Duckworth, J. (2004). Mathematical data processing. *Near-Infrared Reflectance Spectroscopy. Agronomy Monograph*, *44.* (pp. 115−132).

Gac, J. Y., Droubi, A., Fritz, B., & Tardy, Y. (1977). Geochemical behaviour of silica and magnesium during evaporation of waters in Chad. *Chemical Geologist*, *19*, 215−228.

Gillette, D. A., 1999. Physics of Aeolian movement emphasizing changing of the aerodynamic roughness height by saltating grains (the Owen effect). In: Goudie, A.S., Livingstone, I., Stokes, S. (Eds.), Aeolian Environments, Sediments, and Landforms. John Wiley & Sons Ltd., New York, pp. 129–142.

Goetz, A. Z. (2009). Three decades of hyperspectral remote sensing of the Earth: A personal view. *Remote Sensing of Environment*, *113*(1), S5−S16.

Goudie, A. S. (2009). Dust storms: Recent developments. *Journal of Environmental Management*, *90*(1), 89−94.

Green, A., Berman, M., Switzer, P., & Craig, M. D. (1988). A Transformation for Ordering Multispectral Data in Terms of Images Quality with Implications for Noise Removal: *IEEE Transactions on Geoscience and Remote Sensing*, *26*(1), 65−74.

Hapke, B. (1981). Bidirectional reflectance spectroscopy. 1. Theory. *Journal of Geophysical Research*, *86*(B4), 3039−3054.

Hapke, B. W. (1993). *Theory of reflectance and emittance spectroscopy.* New York: Cambridge Univ. Press.

Herrmann, L. (1996). Staubdeposition auf Böden Westafrikas. Eigenschaften der Stäube und ihr Einfluß auf Boden- und Standortseigenschaften. Hohenheimer Bodenkundliche Hefte 36. 239 p.

Herrmann, L., Jahn, R., & Maurer, Th. (2010). Mineral dust around the Sahara — From source to sink. *Journal of Plant Nutrition and Soil Science*. doi:10.1002/jpln.201000095

Herrmann, L., Mounkaila, M., & Graef, F. (2009). Are there valuable pedological palaeoenvironmental indicators in Northern Chad? In Roland Baumhauer, & Jürgen Runge (Eds.), *Holocene Palaeoenvironmental History of the Central Sahara, Palaeoecology of Africa, Vol. 29, An International Yearbook of Landscape Evolution and Palaeoenvironments* (pp. 107−126).

Hunt, G. R. (1977). Spectral signatures of particulate minerals, in the visible and near-infrared. *Geophysics*, *42*, 501−513.

Koren, I., Kaufman, Y., Washington, R., Todd, M., Rudich, Y., Martins, V., et al. (2006). The Bodélé Depression — A single spot in the Sahara that provides most of the mineral dust to the Amazon forest.*Environmental Research Letters*, *1*, 014005. doi:10.1088/1748-9326/1/1/014005 5 pp.

Kratt, C., Calvin, W., & Coolbaugh, M. (2006). Geothermal exploration with Hymap hyperspectral data at Brady–Desert Peak, Nevada. *Remote Sensing of Environment*, *104*, 313−324.

Kruse, F. A., Lefkoff, A. B., Boardman, J. W., Heidebrecht, K. B., Shapiro, A. T., Barloon, J. P., et al. (1993). The spectral image processing system (SIPS) — Interactive visualization and analysis of imaging spectrometer data. *Remote Sensing of Environment*, *44*, 145−163.

Lillesand, T., & Kiefer, R. (2004). *Remote sensing and image interpretation* (Hardback). (Fifth Edition). : John Wiley & Sons978-0471152279 724 pgs.

Maurer, T., Herrmann, L., & Stahr, K. (2010). Wind erosion characteristics of Sahelian surface types. Earth Surface Processes and Landforms. doi: 10.1002/esp.1975

Moreno, T., Querol, X., Castillo, S., Alastuey, A., Cuevas, E., Herrmann, L., et al. (2006). Geochemical variations in aeolian mineral particles from the Sahara–Sahel dust corridor. *Chemosphere*, *65*(2), 261−270.

Mounkaila, M. (2006). Spectral and mineralogical properties of potential dust sources on a transect from the Bodélé Depression (Central Sahara) to the Lake Chad in the Sahel. PhD thesis. University of Hohenheim. Hohenheimer Bodenkundliche Hefte 78.

Mounkaila, M., Herrmann, L., Maurer, Th., Gaiser, Th., & Stahr, K. (2003). Spectral and mineralogical properties of potential dust sources on a transect from Sahara to Sahel in Chad. *Mitteilungen der Deutschen Bodenkundlichen Gesellschaft*, *102*, 743−744.

Pedro, G., Carmouze, J. P., & Velde, B. (1978). Peloidal nontronite formation in recent sediments of Lake Chad. *Chemical Geology*, *23*, 139−149.

Prospero, J. M., Ginoux, P., Torres, O., Nicholson, S. E., & Gill, T. E. (2002). Environmental characterization of global sources of atmospheric soil dust identified with the NIMBUS 7 total ozone mapping spectrometer (TOMS) absorbing aerosol product. *Reviews of Geophysics*, *40*, 1.

Schwanghart, W., & Schütt, B. (2008). Meteorological causes of Harmattan dust in West Africa. *Geomorphology*, *95*(3–4), 412−428.

Tegen, I., & Kohfeld, K. E. (2006). Atmospheric transport of silicon. In V. Ittekkot, D. Unger, C. Humbog, & N. Tac An (Eds.), *The silicon cycle. Human perturbations and impacts on aquatic systems. SCOPE*, *66*. (pp. 81−91) : Island Press.

Warren, A., Chappell, A., Todd, M. C., Bristow, C., Drake, N., Engelstaedter, S., et al. (2007). Dust-raising in the dustiest place on Earth. *Geomorphology*, *92*(1–2), 25−37.

Washington, R., Bouetb, C., Cautenet, G., Mackenzie, E., Ashpole, I., Engelstaedter, S., et al. (2009). Dust as a tipping element: The Bodelé Depression, Chad. *PNAS*. doi: 10.1073/pnas.0711850106

Washington, R., Todd, M. C. (2005). Atmospheric controls on mineral dust emission from the Bode´le´ depression, Chad: The role of the low level jet. *Geophysical Research Letters, 32*, L17701. doi:10.1029/2005GL023597

Washington, R., Todd, M. C., Engelstaedter, S., Mbainayel, S., & Mitchell, F. (2005). Dust and the low-level circulation over the Bodélé Depression, Chad: Observations from BoDEx 2005. *Journal of Geophysical Research*, *111*, D03201. doi:10.1029/2005JD006502

Washington, R., Todd, M. C., Lizcano, G., Tegen, I., Flamant, C., Koren, I., et al. (2006). Links between topography, wind, deflation, lakes and dust: The case of the Bodélé Depression, Chad. *Geophysical Research Letters*, *33*, L09401. doi: 10.1029/2006GL025827

Washington, R., Todd, M., Middleton, N. J., & Goudie, A. S. (2003). Dust-storm source areas determined by the total ozone monitoring spectrometer and surface observations. *Annals of the Association of American Geographer*, *93*, 297−313.

Wright, J. (Ed. and principal author), with contribution from Hastings, D., Jones, W., & Williams (1985). Geology and Mineral Resources of West Africa. Publisher: Boston: Allen & Unwin, London, England.